Earth and Space Science

Key Points:

- The 2021 Mw 5.3 Baicheng earthquake may have involved at least 4 km of surface rupture
- The earthquake may have ruptured with three segments, involving both left-lateral strike-slip and tensional fractures
- The earthquake was a shallow (focal depth 0.5–2 km) left-lateral strike-slip (maximum displacement: 0.79 m) rupture event

Supporting Information:

Supporting Information may be found in the online version of this article.

Correspondence to:

Y. Yao and S. Wen,
yy8096658@126.com;
wenshaoyan999@163.com

Author Contributions:

Conceptualization: Yuan Yao
Data curation: Yuan Yao
Formal analysis: Yuan Yao
Funding acquisition: Yuan Yao, Shaoyan Wen
Investigation: Yuan Yao
Methodology: Yuan Yao, Shaoyan Wen, Liao Yang, Xiaolin Sun, Lili Wang, Zhibin Zhang
Project Administration: Yuan Yao, Shaoyan Wen

A Shallow and Left-Lateral Rupture Event of the 2021 Mw 5.3 Baicheng Earthquake: Implications for the Diffuse Deformation of Southern Tianshan

Yuan Yao[1,2,3] ⓘ, **Shaoyan Wen[1,2]** ⓘ, **Liao Yang[4], Chuanyong Wu[5], Xiaolin Sun[4], Lili Wang[4], and Zhibin Zhang[1,2]**

[1]Xinjiang Pamir Intracontinental Subduction National Field Observation and Research Station, Beijing, China, [2]Urumqi Institute of Central Asia Earthquake, China Earthquake Administration, Urumqi, China, [3]State Key Laboratory of Earthquake Dynamics, Institute of Geology, China Earthquake Administration, Beijing, China, [4]Xinjiang Institute of Ecology, Geography Chinese Academy of Sciences, Urumqi, China, [5]Institute of Disaster Prevention, Academy of Earth Sciences, Langfang, China

Abstract On 24 March 2021, an Mw 5.3 earthquake struck northwest Baicheng, located in the Kuqa fold-and-thrust belt (FTB), northwest China. In the current study, interferometric synthetic aperture radar (InSAR) data were used to investigate the associated fault rupture solution (dip, dip direction, and slip sense), to determine the geometry of the seismogenic structure; the high-resolution images of the surface rupture were obtained using an unmanned aerial vehicle (UAV). This geometric model, along with the co-seismic slip distribution from the InSAR data, and deformation characteristics of co-seismic surface rupture revealed that: (a) it was a shallow event, the focal depth was 0.5–2 km, and the co-seismic slip was distributed in the 0–7 km range with high dip angles (66°, 70°). (b) A 4-km long surface rupture with obvious left-lateral strike-slip was distributed on the surface, and the maximum strike-slip displacement and width were 0.79 and 0.7 m, respectively. This left-lateral strike-slip event indicates that the relative motion between the Tianshan and Tarim blocks is a continuous and diffuse deformation process. The study shows that, when evaluating the earthquake risk of the Kuqa FTB, we should consider both the front position of the fault outburst and the internal compressional salt-related structures, which can also produce moderate to strong earthquakes.

Plain Language Summary The northwest of Baicheng, Xinjiang was struck by an Mw 5.3 earthquake on 24 March 2021, representing the largest event in the Kuqa fold-and-thrust belt in the past 20 years. This event has several intriguing aspects (a) the surface rupture and epicenter (U.S. Geological Survey and China Earthquake Networks Center): did not occur on a mapped fault; (b) the focal depth was 0.5–2 km, characteristic of a shallow earthquake; (c) the seismic rupture characteristics were incongruous with regional strain. Based upon an integrative analysis for interferometric synthetic aperture radar and unmanned aerial vehicle data, we obtained the deformation field, co-seismic slip distribution, and surface rupture. The deformation field was found to be 16.5 km long and 7.7 km wide, while the surface rupture length was 4 km and exhibited characteristics of left-lateral strike-slip deformation. We found an isolated and shallow compressional salt dome below the epicenter, which corresponds well with the rupture characteristics of the source. It is, therefore, believed that the earthquake was caused by rupture of the compressed salt structure. Our study has important implications for understanding the relative geohazard and movement characteristics of the Tarim and Tianshan blocks.

1. Introduction

The sliding distribution of convergent orogenic belt is the key to understanding the tectonic deformation and evolution mechanism of collision orogens (Allen et al., 2017; Alvarado et al., 2016; Beck, 1983; Fu et al., 2002; Molnar, 1988; Thompson et al., 2017; Zhang et al., 2004). Tianshan has been reactivated by the collision of India-Eurasia plate since the Cenozoic era (Avouac & Tapponnier, 1993; Molnar & Tapponnier, 1975; Tapponnier & Molnar, 1979; Yin et al., 1998; Zhang et al., 1996) and it is one of the typical intracontinental convergent orogenic belts in Eurasia (Figure 1a). The frequent occurrence of strong earthquakes and extensive active tectonics are evidence of strong present-day tectonic deformation in the Tianshan (Figure 1a). However, in addition to the crust shortening deformation dominated by the foreland fold-and-thrust belt (FTB) on both sides of the Tianshan

(Abdrakhmatov et al., 1996; Avouac & Tapponnier, 1993; Molnar & Ghose, 2000; Zubovich et al., 2010), a series of large internal strike-slip faults also indicate that the Tianshan is undergoing shear deformation (Shen et al., 2001; Wang and Shen, 2020; Zubovich et al., 2010). For example, the Kemin-Chilik Fault, Nikolave Line, and Maidan Fault all have large left-lateral strike-slip faults in the NE trend (Figure 1a).

On 24 March 2021, a Mw 5.3 earthquake struck Baicheng town, located within the Kuqa Basin, a FTB in the southern Tianshan mountains (Figure 1b). This event caused ∼4 km of surface ruptures at the epicenter (Figures 1c and 1d), massive building damage, and multiple casualties (three deaths). The focal mechanism of the main shock estimated from the China Earthquake Networks Center (CENC) preliminary centroid moment tensor indicated predominantly NEE left-lateral strike-slip motion with a tension component. Different groups provided epicenter locations near 41.81°N and 81.16°E (an uncertainty of ∼10 km; Table 1). The earthquake occurred in the Kuqa FTB, located at the first-row anticline zone of Kuqa FTB.

The 2021 Mw 5.3 Baicheng event is the focus of this study, which is one of the few earthquakes with a Mw < 5.5 that produced surface rupture. As such, in the current study, we summarize the available seismologic, interferometric synthetic aperture radar (InSAR), surface geology, and seismic reflection profiles of this event, thus providing important constraints on the geometry and co-seismic slip of the rupture fault. We then used an unmanned aerial vehicle (UAV) to capture high-resolution aerial photographs (resolution of 2.46 cm/pix) of the surface rupture (length = 4 km), which were subsequently interpreted. Additionally, the distribution characteristics and sliding parameters of surface rupture were obtained. The results can be broadened to characterize other salt-bearing FTBs and are important for enhancing our understanding of the seismic risk of salt-bearing FTBs.

2. Tectonic Setting

2.1. Regional Tectonics

The Tianshan are located in the hinterland of Eurasia and are the product of violent collisions between the Indian plate and Eurasian plate since the late Cenozoic. The region experiences intense deformations and the strongest seismic activity in the Cenozoic continental interior. Per GPS measurements (Abdrakhmatov et al., 1996; Wang and Shen, 2020; Zubovich et al., 2010) and analyses of seismic moment release (Molnar and Ghose, 2000), the region currently exhibits rapid N–S oriented shortening at a rate of ∼20 mm/a in the western Tianshan; this rate decreases gradually to ∼5 mm/a in the easternmost Tianshan, which is consistent with clockwise rotation of the Tarim Basin relative to the Kazakh Platform-Junggar Basin (Avouac & Tapponnier, 1993).

The Tianshan are characterized by widely distributed active thrust-faulting (Figure 1a). Within the mountains, major active thrusts have developed along range-basin boundaries, typically exhibiting moderate-high angles and basement-involved fault geometries (Allen et al., 1999; Ghose et al., 1998; Makarov et al., 2010; Sadybakasov, 1990; Thompson et al., 2002). Along the mountain front, an array of thrust and fold belts have developed due to thrusting of the mountain over the foreland basins. These active structures within and along the mountain front have Late-Quaternary slip rates of 0.1–5.0 mm/a (Charreau et al., 2017; Saint-Carlier et al., 2016; Stockmeyer et al., 2017; Thompson Jobe et al., 2017). In addition to the active thrust faults, several large-scale strike-slip faults are present (Figure 1a), such as the Talas-Fergana Fault, Dzhungarian Fault, Kemin-Chilik Fault, and Nikolave Line, which play a role in accommodating the lateral variation of the horizontal shortening of the mountain.

Between 1812 and 1946, the Tianshan experienced a remarkable sequence of strong earthquakes (Figure 1a; Abdrakhmatov et al., 2016; Molnar and Deng, 1984; Molnar and Ghose, 2000; Kulikova, 2016). In total, six M ≥ 7.5 earthquakes were recorded, including the 1812 M 8.0 Nileke, 1889 M 8.3 Chilik, 1902 Mw 7.7 Atushi, 1906 M 7.7 Manas, 1911 Mw 8.0 Chon Kemin, and 1946 Mw 7.6 Chatakal events. However, since 1947, the mountain has been relatively free from the effects of strong earthquakes, and only one $M \geq 7.0$ event (1992 Mw 7.2 Suusamyr event) was recorded. Among these earthquakes, apart from the 1812 Nileke (M 8.0), 1885 Belovodskoe (M 6.9), 1889 Chilik, and 1911 Chon Kemin events that produced spectacular surface ruptures (Abdrakhmatov et al., 2016; Arrowsmith et al., 2016; Wu et al., 2020), all other earthquakes produced only limited or no surface ruptures.

The 2021 Mw 5.3 Baicheng event occurred within the Baicheng Basin in front of the Southern Tianshan, a foreland basin within the Kuqa FTB (Figures 1a and 1b). The basin is bounded on its northern margin by the Southern

Figure 1. (a) Topography, active structures, and earthquakes ($M \geq 5.0$ during 1800–2020) in the Tianshan region. The red line is the major NE trend strike-slip fault in Tianshan. (b) Topography, active structures, and major earthquakes ($M \geq 5.0$) during 1951–2020 within the Kuqa FTB, according to the CENC seismic catalog. (c) and (d) Satellite image and geologic map of the 2021 Baicheng earthquake epicenter and related fold. Pink circles represent aftershocks (March 24–26, 2021; data from Xinjiang Earthquake Networks Center).

Table 1
Focal Mechanism Solutions of the 2021 Baicheng Main Shock

Agency	Magnitude	Longitude (°)	Latitude (°)	$\phi 1$ (°)	$\delta 1$ (°)	$\lambda 1$ (°)	$\phi 2$ (°)	$\delta 2$ (°)	$\lambda 2$ (°)	d (km)
CENC	Ms = 5.4	81.11	41.7	341	75	180	71	90	15	10
GFZ	Mw = 5.2	81.15	41.77	160	77	167	253	77	12	13
USGS	Mw = 5.3	81.155	41.812							10 ± 1.8

Note. Ms is the surface wave magnitude; Mw is the moment magnitude; ϕi, δi, and λi ($i = 1, 2$) denote the strike, dip, and rake of the two nodal planes, respectively, and d denotes the depth. The CENC data were downloaded from https://news.ceic.ac.cn/index.html?time=1590980075. Helmholtz-Center Potsdam - German Research Center for Geosciences (GFZ) data were downloaded from http://geofon.gfz-potsdam.de/eqinfo/event.php?id=gfz2021ftpu. U.S. Geological Survey (USGS) data were downloaded from https://earthquake.usgs.gov/earthquakes/eventpage/us6000dvwp/origin/detail.

Tianshan Fault (STF) and on its southern margin by the Qiulitag thrust fault. The epicenter was approximately 6 km to the north of the STF, which is a north-dip thrust fault.

2.2. Kuqa Fold-and-Thrust Belt

The Kuqa FTB, located in the southern piedmont of the Tianshan mountains, is predominantly composed of five structural belts trending roughly E–W from north to south: the STF, Tuzima-Kumgeliem anticline belt, Baicheng Basin, Qiulitag structural belt, and Kalayuergun anticline belt (Figure 1b and Gao et al., 2020; Li et al., 2012; Tang et al., 2018; Wang et al., 2011). Two sets of thick salt-gypsum rocks have been deposited in the Kuqa FTB since the Cenozoic, namely, the Paleogene Kumgeliem Formation (E_{1-2km}) and Neogene Jidike Formation (N_{1J}, Izquierdo-Llavall et al., 2018; Li et al., 2012; Pla et al., 2019; Tang et al., 2018). The salt-gypsum rocks in the study area are from the Kumgeliem Formation; these salt structures can be divided into two types: salt diapirs and integrative salt anticlines (Li et al., 2012; Wang et al., 2011). The salt diapirs are unconformable with the surrounding sedimentary strata, and the strata around the salt diapirs exhibit onlapping, downlapping, denudation, and unconformities. When the sedimentary structures are far from the salt diapirs, the parallel bedding of the strata is not deformed, indicating that upwashing of the salt diapir occurs simultaneously with that of the surrounding sedimentary strata (Giles & Lawton, 2002; Rowan et al., 2003).

Considering the abundant oil and gas resources in the Kuqa FTB, petroleum companies have constructed numerous 2D and 3D seismic reflection profiles that reveal the characteristics of underground structures (Gao et al., 2020; Wang et al., 2011). To better determine the seismogenic structure of the Baicheng event, we selected a seismic reflection profile (Figure 1b, Gao et al., 2020) that passed through the epicenter. In the reflection profile, we identified the Laohutai salt dome, the Qiulitag salt thrust, and the Miskantag salt anticline (Figures 2a and 2b). The Paleogene Suweiyi Formation (E_{2-3S}), Neogene Jidike Formation (N_{1J}), and Kangcun Formation
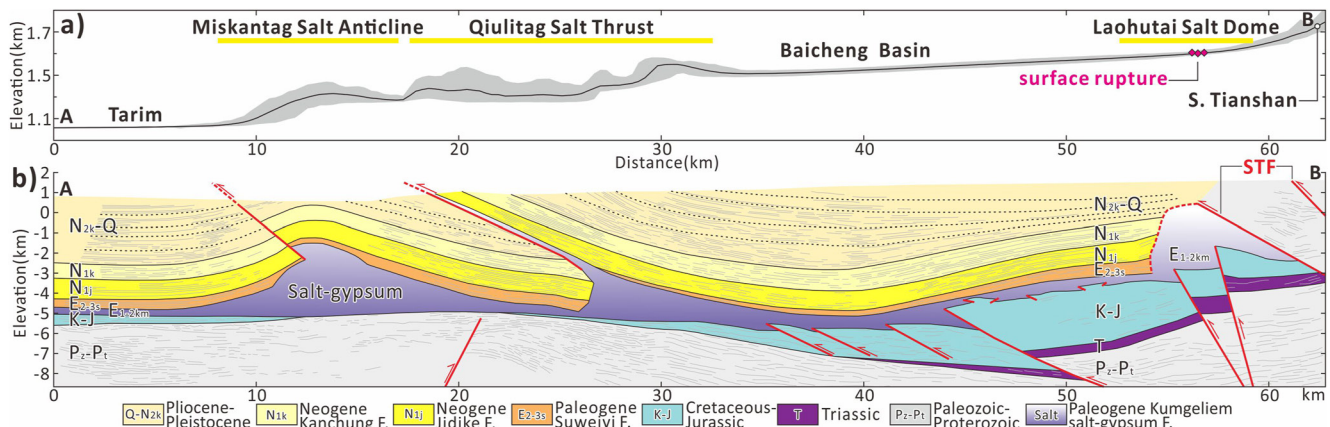

Figure 2. (a) Surface longitudinal section of the seismic reflection profile. (b) Geologic cross sections of the salt structure, Qiulitag salt thrust, and Miskantag anticline, based on the seismic reflection profile (modified from Gao et al., 2020; Wang et al., 2011).

(N_{1K}) were punctured by the Laohutai salt dome, and then covered by the upper Neogene Kuqa Formation (N_{2K}). The thickness of the salt overlying the strata on the south side of the Laohutai salt dome can be divided into upper and lower parts; the Paleogene to Neogene are pre-compressional sedimentary strata, and the Pliocene to Quaternary are compressional growth strata (Figure 2b).

3. The 2021 Baicheng Earthquake

The 2021 Mw 5.3 Baicheng earthquake occurred at 05:14 UTC on 24 March 2021 (Table 1). Its epicenter was located in the northwest of the Baicheng Basin, approximately 6 km away from the STF in the north (Figure 1b). Seismic parameters from different agencies indicated that this event was a left-lateral strike-slip event. The focal mechanisms suggested by the CENC and the Helmholtz-Center Potsdam – German Research Center for Geosciences (GFZ) were similar (Table 1): strike/dip/rake were 71–73°/77–90°/12–15°. These solutions are nearly parallel to the strike of the STF. Due to the sparse seismic stations operating in the region, the focal depth was determined to be 10–13 km (Table 1).

Besides the Mw 5.3 mainshock, a total of 10 aftershocks were recorded for the period of March 24 to 25, 2021, including 5 events with magnitudes ≥3.0 (data from Xinjiang Earthquake Networks Center). These aftershocks, in map view, overlap with the co-seismic rupture patch (Figure 1c). There has been no earthquake with a magnitude >5.0 in the epicenter and adjacent area of the Baicheng event in the historical record (1800–2020). Notably, an Mw 4.9 earthquake occurred in this region on 23 March 2020, and the focal mechanism solution given by the CENC denoted that this was also a left-lateral strike-slip event (Figure 1b).

4. Co-Seismic Deformation Maps

4.1. Co-Seismic Sentinel-1 Interferograms

The two-pass differential InSAR approach (Massonnet et al., 1993; Rosen et al., 2000) was used to process the ascending data acquired by the European Space Agency Sentinel-1A satellite (Yang et al., 2021), while ENVI/SARscape software was used to process the SAR data (https://search.asf.alaska.edu/#/). The ascending image pair was acquired on 20–26 May 2021, with a temporal baseline of 7 days and perpendicular baseline of 56 m. To avoid the phase jumps between adjacent subsequent bursts and improve image pair coherence, repeated azimuth co-registration was performed to achieve a registration accuracy better than 0.1 pixel. The 1-arc s (~30 m) resolution Shuttle Radar Topography Mission digital elevation model (DEM) was used to simulate and remove the topographic phase component (Farr et al., 2007). Adaptive filtering was then adopted for the interferograms (Goldstein & Werner, 1998) to effectively reduce decorrelation noise. Interferogram unwrapping used the minimum cost-flow algorithm (Werner et al., 2002). Finally, the line-of-sight (LOS) displacement fields in Figure 3a were geocoded onto the WGS-84 geographic coordinate. One fringe represents half the wavelength of the C-band SAR data, which is 2.8 cm.

The deformation range was ~16.5 km long and 7.7 km wide (Figure 3b). The deformation field showed two deformation centers, one on each side of the fault, with larger deformation in the east than the west on both sides. The certain degree of decorrelation near the fault indicated that the earthquake caused rupture on the surface. The interferogram fringes far from the fault were continuous and ellipsoidal along the E–W trending seismogenic fault. The maximum deformation was ~16 cm (Figure 3c) on both sides of the fault. The northern deformation in the LOS was positive (moving toward the satellite), whereas the southern deformation was negative. Moreover, there were two positive and negative deformation centers on each side, which agreed with the deformation characteristics of a moderate–strong earthquake. Combined with the regional tectonic setting, it is considered that this event may have occurred on a high-angle strike-slip fault.

4.2. Inversion for Fault Parameters and Slip Distribution Inversion

Inversion of seismic source mechanisms based on geodetic observations is an important means of understanding seismogenic structures. The method of steepest descent (SDM) with constrained least-squares optimization was used to conduct geodetic inversion, which minimizes the root-mean-square misfit between the observations and the model (Wang et al., 2013). Quad-tree decomposition (Jonsson et al., 2002; Wang et al., 2014) was used to down-sample the deformation field to improve computational efficiency and increase the signal-to-noise ratio,
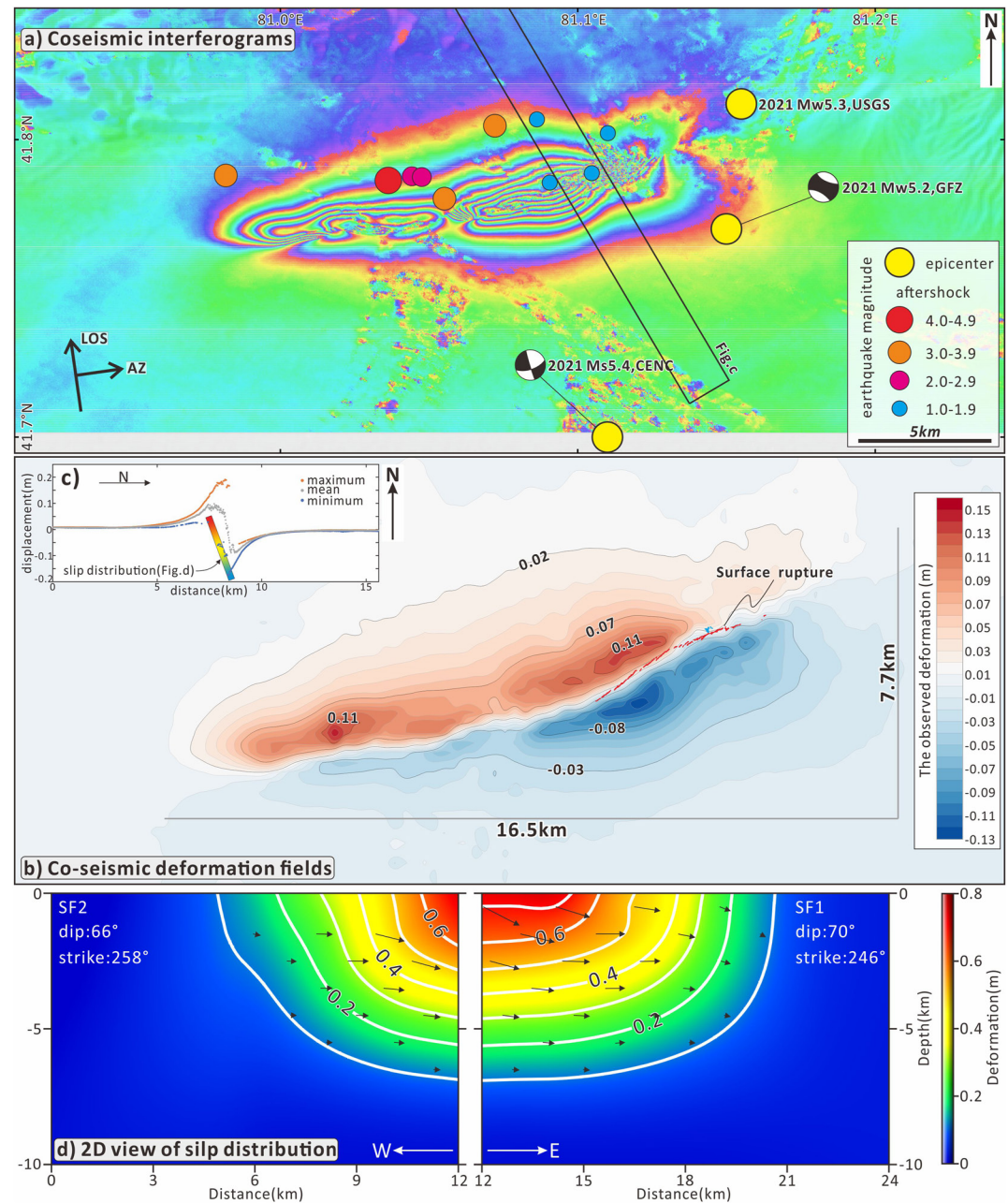
Figure 3. (a) Interferogram of co-seismic deformation from the ascending track of the European Space Agency Sentinel-1A satellite. (b) Co-seismic deformation fields. (c) Profile of co-seismic deformation (location provided in Figure 3a). (d) Slip distribution from joint InSAR ascending observations (7,043 points). According to the interferogram characteristics, the inversion occurs in two sections, with inversion parameters of 70° (dip), 246° (strike), 66° (dip), and 258° (strike).

allowing important and detailed information to be retained as much as possible. Millions of InSAR pixels were reduced to a few thousands after down-sampling, and a total of 7,043 points from the ascending track were used to retrieve the fault geometry parameters and slip distribution.

As revealed by the interferograms, field investigations, and regional tectonic setting, the high dip nodal plane of the focal mechanisms (U.S. Geological Survey, Helmholtz-Center Potsdam – German Research Center for Geosciences) was the preferred initial geometry in the following InSAR-based inversion. Combined with the aforementioned analysis, a fault model was built with two segments with the strike-changed fault plane comprising 1 × 1 km rectangular sub-patches. The fault surface trace was determined by the co-seismic deformation field
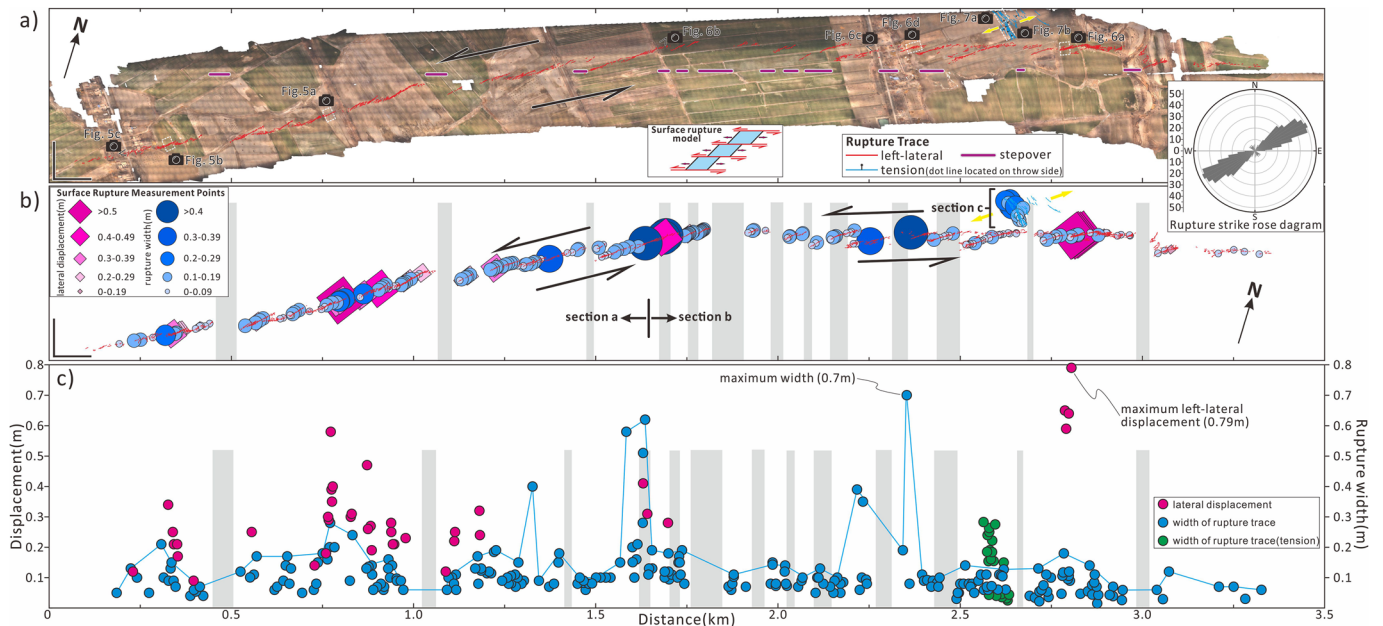
Figure 4. (a) Surface rupture zone of the Baicheng earthquake captured by UAV (13,123 photographs). Red and blue lines indicate strike-slip and extensional surface rupture, respectively. (b) Left-lateral strike-slip displacement and rupture width are represented by blue circles and pink diamonds, respectively. Inset: rose diagram based on the mapped surface rupture, where the dominant trend is N50–70°E. (c) Left-lateral strike-slip and width displacement distribution of surface rupture. Pink, blue, and green dots represent strike-slip displacement, rupture width, and extensional surface rupture width, respectively. The locations are shown in Figure 4a.

and field investigation rupture points. The geometry parameters of the fault model included a strike of ~246° for east sub-fault 1 (SF1) and ~258° for west sub-fault 2 (SF2), lengths of SF1 and SF2 at ~11.5 and 7.5 km along the strike, respectively, and 15-km widths along the down-dip for the two sub-faults (Figure 3d). This model was used to estimate the optimal source parameters, including dip, strike, and rake of fault. The fault slip on each patch was solved using the elastic half-space homogeneous dislocation model (Okada, 1985), assuming a Poisson ratio of 0.25. Through "forward simulation" to simulate the deformation image, and a comparison with the observed deformation field, the parameters were adjusted constantly to obtain the geometric parameters of the fault. The fault model, with a dip of 70° for SF1 and 66° for SF2, closely fit the InSAR observations with a 0.05 smoothing factor.

The slip distribution along the down-dip direction is shown in Figure 3d. Our best-fit inverted slip model showed that the rupture process was controlled by left-lateral strike-slip motion, with a slight normal component and average rake angle of 348° for SF1 and 350° for SF2. Generally, our preferred model had a single-slip asperity pattern, with a significant slip area of ~16 km along the strike and ~7 km along the down-dip direction. The rupture extended to the surface and the peak slip magnitude was up to 0.7 m on SF1, which occurred at ~0.5 km with a 332° rake angle. The seismic moment magnitude estimated by geodetic data was Mw 5.9. The residuals of the optimal slip distribution in the near field were generally <3 cm (Figure S1 in Supporting Information S1) and the data-model correlation was as high as ~98%, indicating that the inversion result was reliable.

5. Co-Seismic Surface Rupture

In this study, we used a DJI M300 UAV (XT2 Pan-Tilt) to obtain aerial photographs (13,123 photographs) of the surface rupture following the Baicheng event on 24–25 March 2021. Per the terrain in the aerial photography area, the sailing height was set to 50 m, the heading overlap rate was 60%, and the lateral overlap rate was 60%. The images were processed indoors using Agisoft Metashape Professional software to generate a high-resolution orthographic Mosaic (Figure 4a) and a DEM (resolution 14–77 cm). The detailed surface rupture zone was then interpreted using the orthographic Mosaic map in ArcGIS software (Data Sets S1 in Supporting Information S1, KMZ File). Because there was no control point in the aerial photography area, the deviation between the

aerial orthographic Mosaic and the actual landform point was less than 6 m. We measured 315 surface rupture observation points based on the orthographic Mosaic and obtained the width and strike-slip displacement distribution map of surface rupture for the Baicheng event (Figures 4b and 4c), in which the observation error was primarily derived from the image resolution. We found 41 left-lateral strike-slip displacements along the rupture zone, using the N–S ridges as a reference (Table S1 in Supporting Information S1). A total of 274 data points were collected for the width of surface rupture (Table S1 in Supporting Information S1). The seismic surface rupture patterns obtained by interpretation of the high-resolution orthophoto images showed that the 2021 Baicheng earthquake produced co-seismic surface ruptures on the piedmont alluvial fan (1,500–1,700 m above sea level, which is now farmland) in southern Tianshan, with a total length of ~4 km. Although the surface fracture generally exhibited a linear distribution, left-lateral en-echelon traces divided by stepovers were also observed.

To define the surface rupture characteristics and co-seismic displacement more accurately, we comprehensively analyzed the source parameters and InSAR inversion results. The surface rupture of the Baicheng earthquake was characterized by sinistral strike-slip and tensional fractures, and the main rupture zone was a sinistral strike-slip fault with a strike of N50–70°E. A group of E–W tensile fractures developed along 2.6 km of the rupture zone, forming a graben with a strike of S125–135°E (Figure 4a). According to the change in the trend and its spatial distribution, the surface rupture was divided into three sections from west to east: sections a, b, and c, successively (Figure 4b). Each rupture section was composed of several secondary ruptures. The surface rupture was geometrically simple and distinguished by 13 major steps, the widest of which was ~100 m.

Section a: The rupture zone in this section reached the Muzart River to the west (Figure 1c), with an overall trend of N50°E and a total length of approximately 1.6 km (Figure 4b). The rupture in this section was characterized by a linear strike slip and was separated by three main stepovers. At observation points 5a and 5b (Figure 4a), the north–south ridge was dislocated left-laterally, with the left-lateral displacement being 0.52–0.59 m and 0.20–0.30 m, and the depth being approximately 0.63 m (Figure 5d). Along the rupture zone, houses within a width of 200 m were severely damaged or even collapsed (Figure 5c).

Section b: This section was approximately 2 km in length, with an overall trend of N70°E (Figure 4b). The rupture in this section was dominated by tensile ruptures (Figures 6b and 6d), showing left-lateral en-echelon distribution characteristics, separated by 10 main stepovers, and locally developed with obvious sinistral strike-slip characteristics (Figures 6a and 6c). At the observation point 6a (Figure 4a), the left-lateral dislocation of the rupture zone broke the north–south ridge, and the largest left-lateral dislocation in the whole rupture zone was 0.79 ± 0.1 m. At the observation point 6b, there were a series of tensile cracks with a maximum width of ~0.7 m.

Section c: This section was located 2.6 km from the rupture zone, with a total length of approximately 0.2 km and an overall trend of N45°W (Figures 4a and 4b). It consisted of ruptures that dipped eastward and westward, forming a graben (Figures 7a and 7b). The tension motion's direction of this graben was N35°E, which was nearly consistent with the motion of direction of surface rupture in section a. This showed that the northern wall of the rupture was an active wall, which slid horizontally to the east and formed a series of left-lateral strike-slip ruptures on the surface.

In addition, it should be emphasized that the surface rupture terminated westward on the eastern bank of the Muzart River (Figure 1c). However, the co-seismic deformation field of InSAR (Figure 5b) indicated that this earthquake may have caused surface rupture with a length of approximately 10 km, but we only found a surface rupture with a length of ~4 km (Figure 5b), which was far from the results of InSAR. The main reason is that the west side of the co-seismic deformation field is located in the bed of the Muzart River, and this part belongs to the region upstream of the river and contains a lot of boulders. This means that even when a rupture occurs, it can be obscured or covered by boulders, making it impossible to detect through field surveys and drone images. In addition, due to the site effect, the 0–3 km depth zone is mostly the velocity enhancement zone, while the 3–14 km depth zone is the velocity-weakening zone; the latter generally corresponds to the high-speed sliding phenomenon of seismic ruptures, while the former is not conducive to the expansion of seismic ruptures. Therefore, if there is thick (thousands of meters) unconsolidated sedimentary cover near the surface, when it ruptures into a velocity enhancement zone, it will be quickly or slowly transformed with a certain width and a large wavelength, and diffusion deformation will occur with relative motion or rotation among the loose particles (Figure 8, Bonilla, 1988; Tang et al., 2015). For example, in the 1976 Tangshan Ms 7.8 earthquake, due to the

Figure 5. UAV images and photographs of surface rupture in segment (a). (a) The left-lateral displacement is 0.55 m. (b) Left-lateral displacement is 0.24–0.29 m. (c) Severe damage and collapse occurred as the surface ruptured through the house. (d) The depth of surface rupture in section a is ∼0.6 m.

huge thickness of Quaternary sedimentary cover, it was difficult for the rupture to break through the surface, and only 8 km of surface rupture occurred on the surface (Long et al., 2006).

6. Discussion

6.1. The Shallow Rupture Event

Earthquakes occur at various depths, from the shallow crust to the base of the mantle transition zone. Destructive earthquakes are mostly shallow, concentrated in the upper crust of continents and in the shallow parts of megathrust faults (Fialko et al., 2005; Kaneko and Fialko, 2011; Xu et al., 2016). Focal depth plays an important role in the intensity of the ground motion, which determines the destructive power of similar earthquakes. Scholz (1998) proposed that the rupture began at a deeper depth, in an environment wherein a greater stress drop could be expected to propagate across the fault plane. Conversely, due to insufficient strain energy, fractures starting from shallow depths with lower friction strength and stress drop were inhibited. However, moderate to large earthquakes can indeed occur at very shallow depths, such as the Meckering Ms 6.8 earthquake in western Australia in 1968, where the main shock and most aftershocks were located 1–2 km below the surface (Langston, 1987).

The 2021 Baicheng event is the largest earthquake that has occurred in the past two decades in the Kuqa FTB, causing several casualties and substantial property loss. However, previous geological and geomorphological surveys have not found any fault traces around the epicenter of this earthquake, making it difficult to effectively
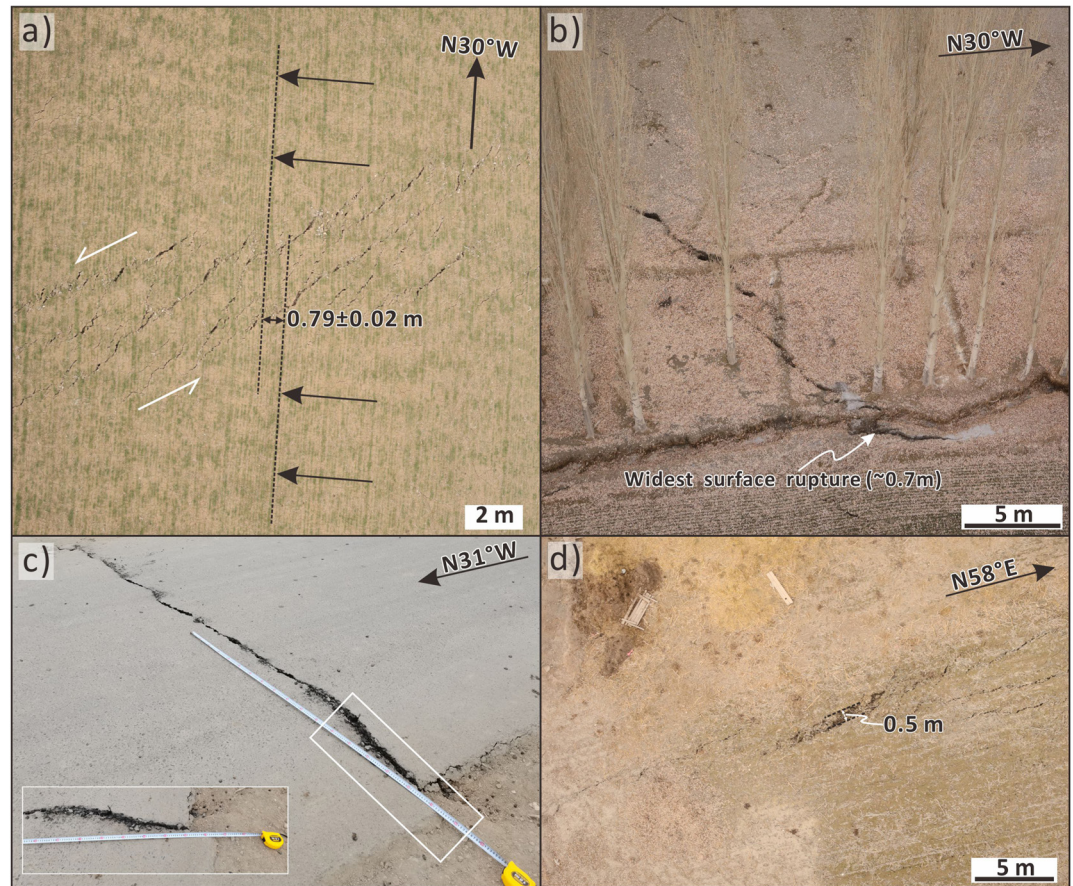
Figure 6. UAV images and photographs of surface rupture in segment (b). (a) The maximum left-lateral displacement is 0.79 m (the markers are ridges). (b) and (c) Surface rupture dominated by tensional stress, with widths of 0.7 and 0.5 m, respectively. (d) Left-lateral dislocation characteristics on asphalt and cement roads. The locations are shown in Figure 4a.

determine its seismogenic structure. We projected the epicenter location, focal mechanism, co-seismic surface rupture, and InSAR co-seismic deformation field on to the plane, and subsequently projected the seismic reflection profile and InSAR slip distribution to the plane location and depth to analyze the seismogenic structure of the 2021 Baicheng earthquake (Figure 9a). The nucleation depth of this event was 0.5–2 km, and it propagated upward to the surface and downward to ∼7 km (Figure 3d). The maximum value of the slip distribution obtained by InSAR inversion was 0.7 m (Figure 3d), approximately 0.5 km near the surface, which was highly consistent with the maximum left-lateral dislocation (0.79 m) measured for the surface rupture (Figure 4c). Thus, the 2021 Baicheng earthquake was a shallow or ultra-shallow seismic event.

It is generally believed that earthquakes should only occur under velocity-weakening (Scholz, 1998). In contrast, rock velocity-strengthening and frictional resistance increase with slip rate at depths shallower than 2–3 km, which are not conducive to fault acceleration (Blanpied et al., 1998). However, the nucleation location and major rupture area of the Baicheng event were located in the Laohutai salt dome, at a depth of ∼1 km (Figure 2b). Although the strength of gypsum rock is lower than that of other rocks (Li et al., 2012), this is not enough to be the cause of rupture and earthquakes; rapid extrusion can make the relatively weak salt rock have strong friction, and the relatively weak plastic deformation indicates high brittleness (Couzens-Schultz et al., 2003). We propose a conceptual structural model for fault motion during the earthquake (Figure 9b). The continuous southward movement of the southern Tianshan mountains squeezed the gypsum-salt rock in the Kuqa FTB, whereby rapid stress accumulation led to brittle fracture of the originally weak gypsum-salt rock, resulting in an earthquake. In the surface geological survey, we did not detect any fault traces and could not designate the seismogenic structure by the fault name; therefore, we designated this event as a "compressional salt tectonic earthquake" (Figure 9b).
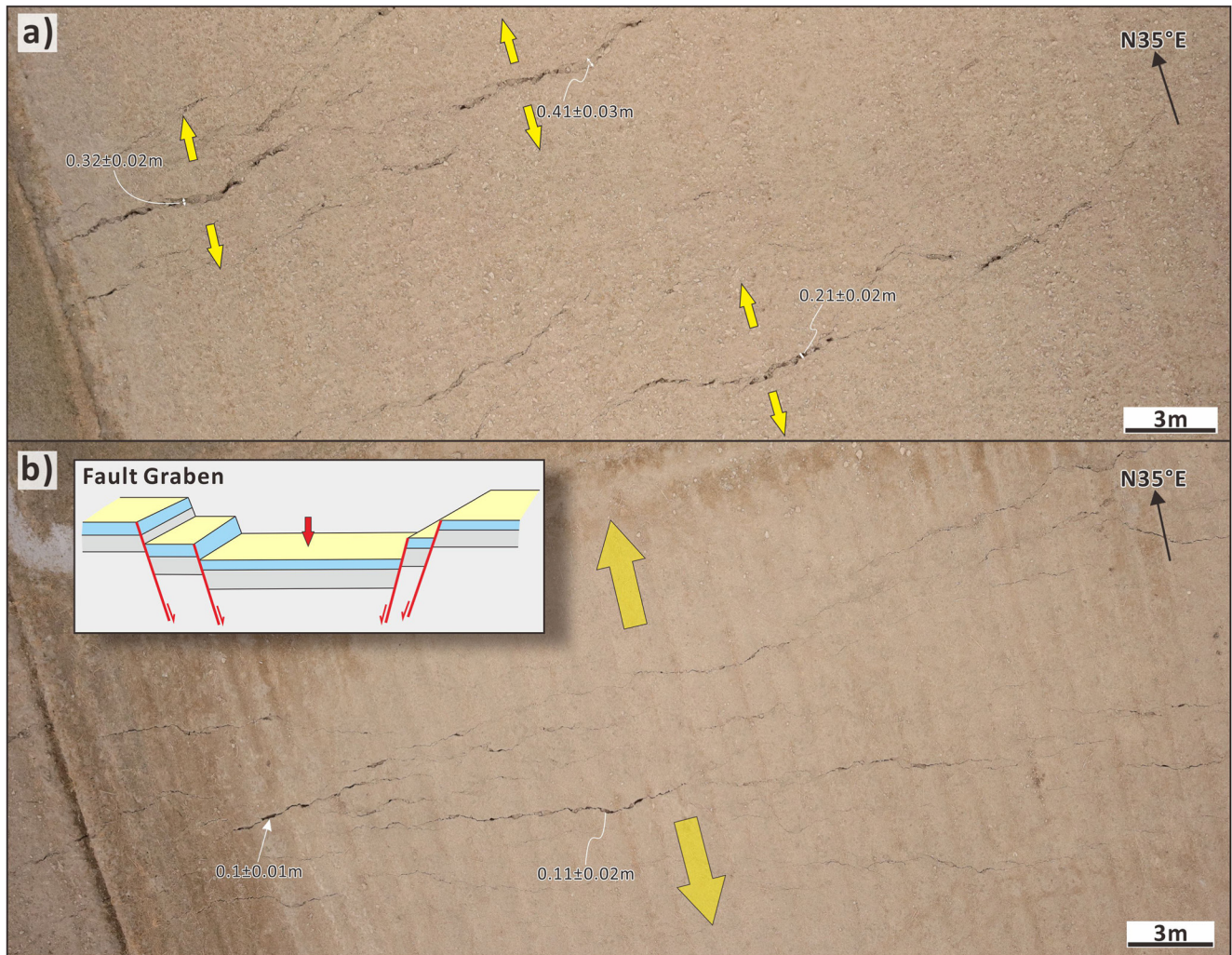
Figure 7. UAV images of surface rupture in segment (b). (a) Tensile surface rupture; widths are 0.21, 0.32, and 0.41 m, respectively. (b) The ruptures dip eastward and westward, forming a graben. The tension motion's direction of this graben is N35°E.
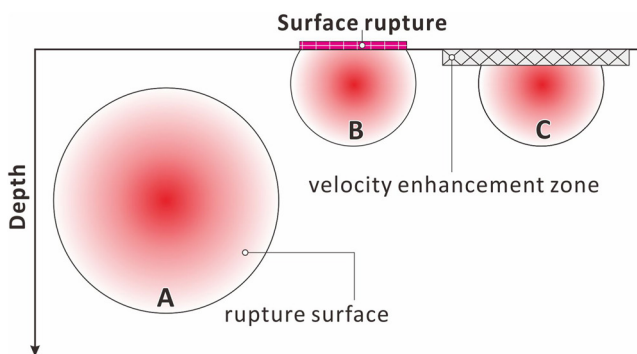

Figure 8. Diagram illustrating the control of focal depth on surface rupture. The velocity enhancement zone is not conducive to the expansion of seismic rupture (modified from Tang et al., 2015).

6.2. Left-Lateral Strike-Slip Rupture Event: Clockwise Rotational Diffuse Deformation of the Tarim Block

The collision between the Indian plate and the Eurasian plate not only caused the uplift of the Tibetan Plateau, but also caused the Tarim Block, Tianshan, and Junggar to continuously push northward, forming the present tectonic framework. The northward movement of the Tibet Plateau pushed the Tarim Block northward at 13.8 mm/a and the Junggar Block northward at 6.4 mm/a (Wang and Shen, 2020). This differential movement was absorbed by the shortening of the crust across the Tianshan and the clockwise rotation of the Tarim Block. The rotation rate of the Tarim Block is approximately $0.63 \pm 0.017°$/Ma (Wang and Shen, 2020), which is adapted to the south-north shortening rate from the Tibet Plateau, increasing eastward, and from the Tianshan, increasing westward.

The Tarim Block is surrounded by large strike-slip faults and thrust nappe structures. The southern boundary of the basin is the famous Altyn-Tagh large left-lateral strike-slip fault ($\sim$2,000 km long), and the northern boundary is the STF (Figure 1a). A series of FTBs, such as the Kashgar FTB, Kepingtagh
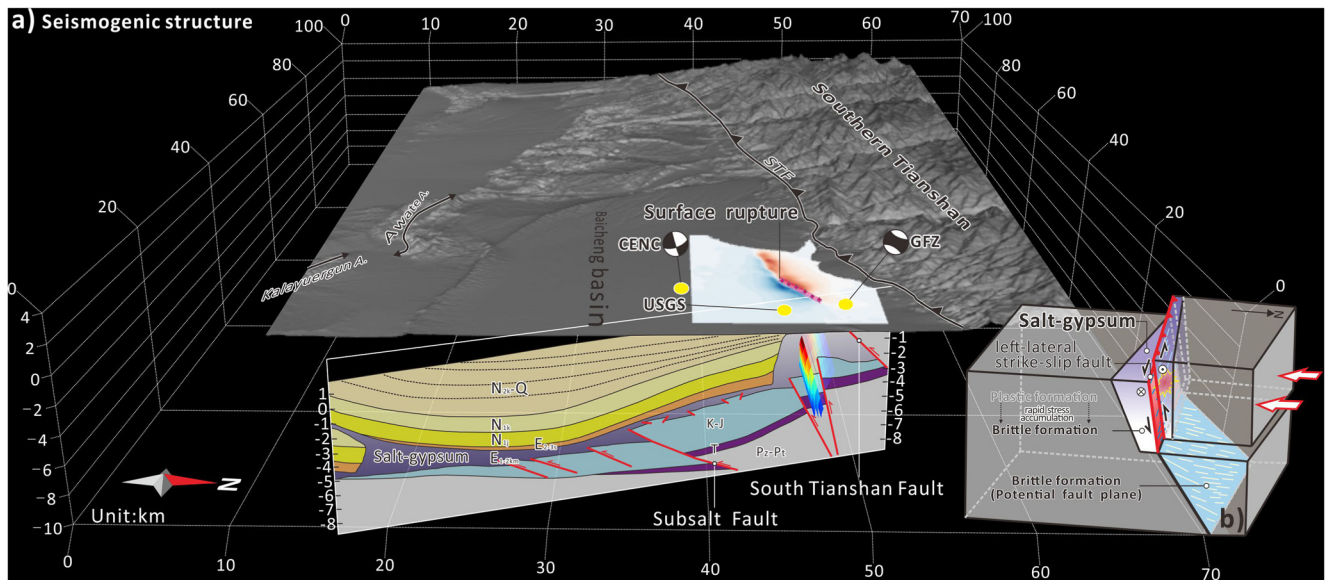
Figure 9. (a) Seismotectonic structure of the 2021 Mw 5.3 Baicheng event. Fault and surface rupture distribution are shown in Figures 1b and 4a. Stratigraphic and fault morphology is derived from Figure 2b. (b) Conceptual structural model of fault motion during the Baicheng event.

FTB, and Kuqa FTB (Figure 1a), are distributed in the foreland basin–mountain area. The left-lateral sliding rate of the western and middle segments of the Altyn-Tagh Fault is 10–12 mm/a (Cowgill et al., 2009; Gold et al., 2009, 2017). However, the STF is usually characterized by a thrust fault with a high angle (Wu et al., 2019; Yao et al., 2018), yet the western segment (Maidan Fault) showed more obvious left-lateral strike-slip characteristics (Figure 1a). The length of the Maidan Fault is approximately 400 km, which is a left-lateral strike-slip fault with a high dip angle (50–60°). Since the Late Quaternary, the left-lateral strike-slip rate is 1.56 ± 0.64 mm/a, and the south-north shortening rate is 1.19 ± 0.25 mm/a (Wu et al., 2019). Obviously, the activity characteristics and slip rate of the STF are insufficient to match the Altyn-Tagh Fault to absorb the clockwise deformation of the Tarim Block. Strike-slip faults usually act as transform structures to accommodate structural deformation (Molnar & Tapponnier, 1975). It is worth mentioning that a series of east-west left-lateral strike-slip faults also developed in the hinterland of Tianshan. In northern Tianshan, the left-lateral strike-slip rate of the Kemin-Chilik Fault since the Late Quaternary is approximately 2 mm/a (Zhou, 2013), and the adjacent foreland thrust belt also extends tens of kilometers to the Kazakh platform (Figure 1a, Goode et al., 2014; Jourdon et al., 2017; Selander et al., 2012). The Kemin-Chilik Fault not only acts as the central structure of the north–south contractional tectonic system of the Tianshan, but also absorbs the clockwise rotation deformation of the Tarim Block by the left-lateral strike-slip motion. In central Tianshan, the Nikolave Line (Figure 1a) is a NEE-trending active Holocene fault with a left-lateral strike-slip rate of approximately 2.5 mm/a (Wu et al., 2014) and a thrusting rate of approximately 1.5 mm/a (Thompson et al., 2002; Wu et al., 2019). The Nikolave Line also acts as the center of another north–south contractional tectonic system, and its left-lateral strike-slip motion also absorbed the clockwise rotation deformation of the Tarim Block.

The 2021 Baicheng event was a shallow earthquake caused by the rupture of compressional salt tectonics in the Kuqa FTB. The focal depth was 0.5–2 km and the rupture reached upward to the surface and the deep rupture reached 7 km. The co-seismic deformation field by InSAR showed that the deformation range of this earthquake was 16.5 km long and 7.7 km wide (Figure 5b). We also found a surface rupture with a length of 4 km (Figures 1c and 1d), with a significant left-lateral strike-slip feature and a maximum strike-slip displacement of 0.79 m (Figures 3 and 4a). The location of the surface rupture and epicenter is not on the previously mapped fault and is also approximately 6 km away from the STF to the north (Figure 1b). This means that there is a significant accumulation of left-lateral strike-slip strain in the region, which is not in accordance with the stress environment of the Kuqa FTB.

As mentioned above, although the STF is the northern boundary between the Tarim Block and the Tianshan, the clockwise rotation deformation of the Tarim Block is not completely absorbed by it, but by multiple left-lateral
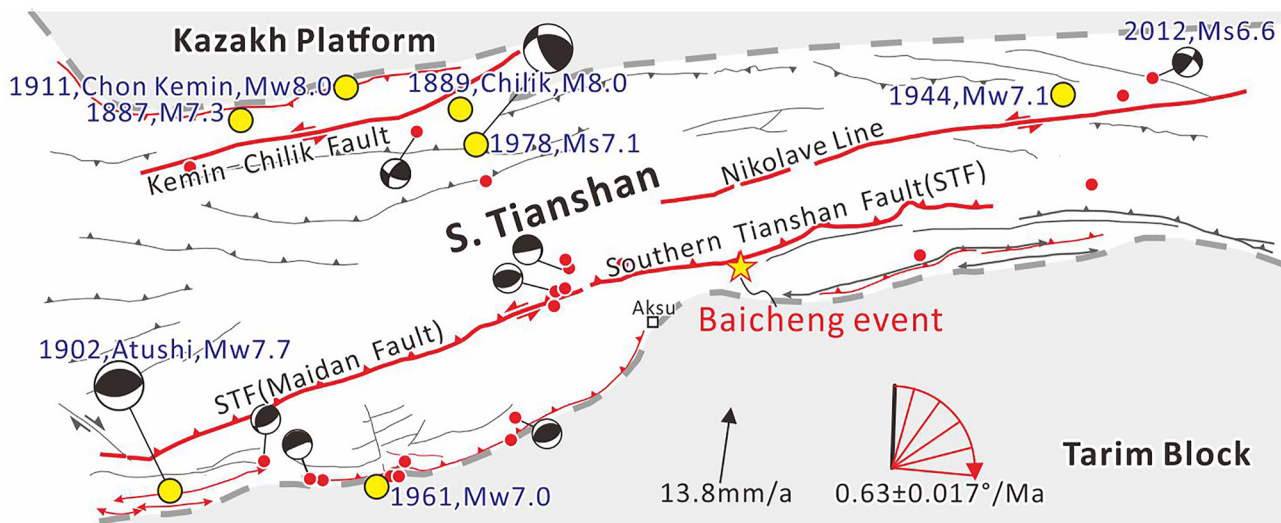
Figure 10. Schematic diagram of tectonic deformation in the Tianshan and Tarim block. The 2021 Mw 5.3 Baicheng event indicates that the relative motion between the Tianshan and Tarim block is a continuous and diffuse deformation process.

strike-slip faults with a high dip angle distributed in the hinterland of Tianshan (Figure 10). For example: the Maidan Fault (STF), Kemin-Chilik Fault, and Nikolave Line together regulate the clockwise rotation deformation of the Tarim Block. The FTBs distributed at the basin-mountain junction, such as the Kashgar, Kepingtagh, and Kuqa FTBs, absorbed the shortening deformation of the northward nappe of the Tarim Block (Figure 1a). Therefore, the current tectonic deformation of the Tianshan and Tarim blocks are more diffuse and continuous, which is clearly different from the more rigid blocks in the Chinese mainland, such as the Qaidam, Ordos, and Yangtze blocks (Zhang et al., 2003). It more closely resembles the Bayan Har Block, with a diffuse and continuous deformation process, and the secondary fault (Kunlunshankou–Jiangcuo Fault, Jiangcuo segment), previously thought to be within the block, was the seismogenic structure of the Madoi Ms 7.4 earthquake in 2021 (Li et al., 2021; Zhan et al., 2021). Obviously, the 2021 Baicheng left-lateral strike-slip rupture event represents an earthquake case that best reflects the diffuse and continuous deformation of the Tianshan and Tarim blocks.

6.3. Implications for Seismic Risk of the Salt-Bearing FTB

The Kuqa FTB experiences some of the strongest tectonic movement in the piedmont regions of the southern Tianshan mountains, with many destructive earthquakes occurring throughout history (Zhang et al., 2003). Previous results, obtained by GPS and geological methods, show that the Kuqa FTB has been pushed southward by ~6 mm/a from the southern Tianshan (Hubert-Ferrari et al., 2007; Wang and Shen, 2020; Yang et al., 2008). Notably, the frequency of moderate/strong earthquakes contrasts with this strong tectonic movement, indicating that the region may be at risk from strong earthquakes.

The Baicheng event was a unique earthquake that occurred in an area with no trace of a surface fault and caused a 4-km long rupture. This study concludes that this was a left-lateral strike-slip earthquake caused by rupture of a buried compressional salt-related structure. Previous studies (Gao et al., 2020; Izquierdo-Llavall et al., 2018; Pla et al., 2019; Wang et al., 2011) have researched salt tectonics in the Kuqa FTB, revealing large areas of compressional salt-related structures that control the growth of multiple rows of anticlines through regional detachment (Figure 1e) and affect the deposition and deformation of overlying strata, owing to upward fluctuations and penetrations caused by differences in density. Hence, the burial depth of these compressional salt-related structures is typically shallow.

Rapid stress accumulation can cause brittle fracture of originally weak salt-gypsum rock and produce earthquakes (Canérot et al., 2005; Couzens-Schultz et al., 2003). Thus, the compressional salt-related structures in the salt-bearing FTB can produce moderate and strong earthquakes. Interestingly, isolated compressional salt-related structures have developed within the salt-bearing FTB, which have accumulated large amounts of southward-pushing strain in the southern Tianshan mountains. As their burial depth is relatively shallow, rupture

may occur during shallow or ultra-shallow earthquakes. In addition to the 2021 Baicheng event, another Ms 5.0 (CENC) left-lateral strike-slip earthquake occurred in this region on 23 March 2020 (Figure 1b). Although this earthquake did not cause surface rupture or the loss of life or property, we cannot ignore the seismic risk from such "compressional salt tectonic earthquakes." Among the hundreds of known salt-bearing basins with salt structures in the world, the basins with compressional salt structures are mainly distributed near 30°N (Hudec & Jackson, 2003). Compressional salt structures can be developed at the slope foot of the passive continental margin (Jackson et al., 2008; Schuster, 1995; Worrall and Snelson, 1989), convergent plate boundary (Canérot et al., 2005; Cotton and Koyi, 2000; Letouzey et al., 1995), and inversion rift basin (Letouzey et al., 1995; Roca et al., 2006). At the convergence plate boundary, the strong extrusion causes the strata to become deformed along the weak detachment (salt-gypsum) in the foreland area and form the thin and thick compressional salt tectonic. In addition, foreland basins tend to be densely populated and economically developed. If a similar shallow earthquake occurs in this area, it may lead to immeasurable loss of life and property. Therefore, when evaluating the seismic risk of the salt-bearing FTB, it is crucial to also consider the influence of salt tectonics.

7. Conclusions

The 2021 Mw 5.3 Baicheng earthquake is a rare example of an earthquake with a magnitude of <5 that can produce surface rupture. In this study, we used InSAR and UAV methods to obtain the slip distribution, deformation, and distribution characteristics of surface rupture. The results of this study illustrate important insights into the seismic activity, shallow co-seismic surface rupture, and shear deformation of Tianshan. Our major conclusions include:

1. The deformation range of this earthquake was 16.5 km long and 7.7 km wide. The focal depth was 0.5–2 km, and the rupture reached upward to the surface and downward to 7 km, with a rupture surface dip of 66° and 70°
2. This event formed a 4-km long surface rupture zone in an area with no traces of surface faults. The rupture zone is characterized by a left-lateral strike-slip, and the maximum strike-slip displacement and width of surface rupture are 0.79 and 0.7 m, respectively
3. This left-lateral strike-slip rupture event indicates that the relative motion between the Tianshan and Tarim blocks is a continuous and diffuse deformation process

Data Availability Statement

The InSAR slip model and UAV survey data are stored in Zenodo and can be accessed online (https://doi.org/10.5281/zenodo.5348603). Sentinel-1 SAR images can be accessed from the European Space Agency (https://search.asf.alaska.edu).

References

Abdrakhmatov, K. E., Walker, R. T., Campbell, G. E., Carr, A. S., Eliott, A., Hillemann, C., et al. (2016). Multisegment rupture in the 11 July 1889 Chilik earthquake (Mw8.0-8.3), Kazakh Tien Shan, interpreted from remote sensing, field survey, and paleoseismic trenching. *Journal of Geophysical Research*, *121*, 4615–4640. https://doi.org/10.1002/2015JB012763

Abdrakhmatov, K. Y., Aldazhanov, S. A., Hager, B. H., Hamburger, M. W., Herring, T. A., Kalabaev, K. B., et al. (1996). Relatively recent construction of the Tien Shan inferred from GPS measurements of present-day crustal deformation rates, *Nature*, *384*, 450–453. https://doi.org/10.1038/384450a0

Allen, M. B., Vincent, S. J., & Wheeler, P. J. (1999). Late Cenozoic tectonics of the Kepingtage thrust zone: Interactions of the Tien Shan and Tarim Basin, northwest China. *Tectonics*, *18*, 639–654. https://doi.org/10.1029/1999tc900019

Allen, M. B., Walters, R. J., Song, S. G., Saville, C., Paola, N. D., Ford, J., et al. (2017). Partitioning of oblique convergence coupled to the fault locking behavior of fold-and-thrust belts: Evidence from the Qilian Shan, northeastern Tibetan Plateau. *Tectonics*, *36*, 1679–1698. https://doi.org/10.1002/2017TC004476

Alvarado, A., Audin, L., Nocquet, J. M., Jaillard, E., Mothes, P., Jarrín, P., et al. (2016). Partitioning of oblique convergence in the Northern Andes subduction zone: Migration history and the present-day boundary of the North Andean Sliver in Ecuador. *Tectonics*, *35*, 1048–1065. https://doi.org/10.1002/2016TC004117

Arrowsmith, J. R., Crosby, C. J., Korzhenkov, A. W., Mamyrov, E., Povolotskaya, I., Guralinik, B., & Landgraf, A. (2016). Surface rupture of the 1911 Kebin (Chon–Kemin) earthquake, northern Tien Shan, Kyrgyzstan. *Geological Society London Special Publications*, *432*, 233–253. https://doi.org/10.1144/SP432.10

Avouac, J. P., & Tapponnier, P. (1993). Kinematic model of active deformation in central Asia. *Geophysical Research Letters*, *20*(10), 895–898. https://doi.org/10.1029/93GL00128

Beck, M. (1983). On the Mechanism of tectonic transport in zones of oblique subduction. *Tectonophysics*, *93*(12), 1–11. https://doi.org/10.1016/0040-1951(83)90230-5

Blanpied, M. L., Marone, C. J., Lockner, D. A., Byerlee, J. D., & King, D. P. (1998). Quantitative measure of the variation in fault rheology due to fluid-rick interactions. *Journal of Geophysical Research: Solid Earth*, *103*(B5), 9691–9712. https://doi.org/10.1029/98jb00162

Bonilla, M. G. (1988). Minimum earthquake magnitude associated with coseismic surface faulting. *Bulletin of the Association of Engineering Geologists*, *25*(1), 17–29. https://doi.org/10.2113/gseegeosci.xxv.1.17

Canérot, J., Hudec, M. R., & Rockenbauch, K. (2005). Mesozoic diapirism in the Pyrenean orogen: Salt tectonics on a transform plate boundary. *AAPG Bulletin*, *89*(2), 211–229. https://doi.org/10.1306/09170404007

Charreau, J., Saint-Carlier, D., Dominguez, S., Lavé, J., Blard, P.-H., Avouac, J.-P., et al. (2017). Denudation outpaced by crustal thickening in the eastern Tianshan. *Earth and Planetary Science Letters*, *479*, 179–191. https://doi.org/10.1016/j.epsl.2017.09.025

Cotton, J. T., & Koyi, H. A. (2000). Modeling of thrust fronts above ductile and frictional detachments: Application to structures in the salt range and potwar plateau, Pakistan. *GSA Bulletin*, *112*(3), 351–363. https://doi.org/10.1130/0016-7606(2000)112<351:motfad>2.0.co;2

Couzens-Schultz, B., Vendeville, B., & Wiltschko, D. (2003). Duplex style and triangle zone formation: Insights from physical modelling. *Journal of Structural Geology*, *25*, 1623–1644. https://doi.org/10.1016/S0191-8141(03)00004-X

Cowgill, E., Gold, R. D., Chen, X., Wang, X.-F., Arrowsmith, J. R., & Southon, J. R. (2009). Low Quaternary slip rate reconciles geodetic and geologic rates along the Altyn Tagh fault, northwestern Tibet. *Geology*, *37*, 647–650. https://doi.org/10.1130/g25623a.1

Farr, T. G., Rosen, P. A., Caro, E., Crippen, R., Duren, R., Hensley, S., et al. (2007). The Shuttle radar Topography Mission. *Reviews of Geophysics*, *45*, RG2004. https://doi.org/10.1029/2005rg000183

Fialko, Y., Sandwell, D., Simons, M., & Rosen, P. (2005). Three-dimensional deformation caused by the Bam, Iran,earthquake and the origin of shallow slip deficit. *Nature*, *435*, 295–299. https://doi.org/10.1038/nature03425

Fu, B. H., Ninomiya, Y., & Guo, J. M. (2002). Slip partitioning in the northeast Pamir-Tian Shan convergence zone. *Tectonophysics*, *483*, 344–364. https://doi.org/10.1016/j.tecto.2009.11.003

Gao, L., Wang, X., & Rao, G. (2020). Two-dimensional balanced restoration of salt structures and analysis of restored cross sections in the Western Kuga depression. *Acta Geologica Sinica*, *94*(6), 1727–1739. (in Chinese with English abstract).

Ghose, S., Hamburger, M. W., & Ammon, C. J. (1998). Source parameters of moderate-sized earthquakes in the Tien Shan, central Asia from regional moment tensor inversion. *Geophysical Research Letters*, *25*, 3181–3184. https://doi.org/10.1029/98GL02362

Giles, K. A., & Lawton, T. F. (2002). Halokinetic sequence stratigraphy adjacent to the El Papalote diapir, northeastern Mexico. *AAPG Bulletin*, *86*(5), 823–840. https://doi.org/10.1306/61EEDBAC-173E-11D7-8645000102C1865D

Gold, R. D., Cowgill, E., Arrowsmith, J. R., & Friedrich, A. M. (2017). Pulsed strain release on the Altyn Tagh fault, northwest China. *Earth and Planetary Science Letters*, *459*, 291–300. https://doi.org/10.1016/j.epsl.2016.11.024

Gold, R. D., Cowgill, E., Arrowsmith, J. R., Gosse, J., Chen, X., & Wang, X.-F. (2009). Riser diachroneity, lateral erosion, and uncertainty in rates of strike-slip faulting: A case study from Tuzidun along the Altyn Tagh Fault, NW China. *Journal of Geophysical Research*, *114*, B04401. https://doi.org/10.1029/2008JB005913

Goldstein, R., & Werner, C. (1998). Radar interferogram filtering for geophysical applications. *Geophysical Research Letter*, *25*, 4035–4038. https://doi.org/10.1029/1998gl900033

Goode, J. K., Burbank, D. W., & Ormukov, C. (2014). Pliocene-Pleistocene initiation, style, and sequencing of deformation in the central Tien Shan. *Tectonics*, *33*, 464–484. https://doi.org/10.1002/2013TC003394

Hubert-Ferrari, A., Suppe, J., Gonzalez-Mieres, R., & Wang, X. (2007). Mechanisms of active folding of the landscape (southern Tian Shan, China). *Journal of Geophysical Research*, *112*, B03S09. https://doi.org/10.1029/2006JB004362

Hudec, M. R., and Jackson, M. P. (2003). Structural segementation, inversion, and salt tectonics on a passive margin: Evolution of the Inner Kwanza Basin, Angola. *GSA Bulletin*, *114* (10): 1222–1244.

Izquierdo-Llavall, E., Roca, E., Xie, H., Pla, O., Muñoz, J. A., Rowan, M. G., et al. (2018). Influence of overlapping décollements, syntectonic sedimentation, and structural inheritance in the evolution of a contractional system: The central Kuqa fold-and-Thrust Belt (Tian Shan Mountains, NW China). *Tectonics*, *37*(8), 2608–2632. https://doi.org/10.1029/2017TC004928

Jackson, M. P. A., Hudec, M. R., Jennette, D. C., & Kilby, R. E. (2008). Evolution of the cretaceous astrid thrust belt in the ultradeep-water lower Congo basin, Gabon. *AAPG Bulletin*, *92*(4), 487–511. https://doi.org/10.1306/12030707074

Josson, S., Zebkeer, H., Segall, P., & Amelung, F. (2002). Fault slip distribution of the 1999 Mw 7.1 Hector Mine, California, earthquake, estimated from Satellite Radar and GPS measurements. *Bulletin of the Seismological Society of America*, *92*(4), 1377–1389. https://doi.org/10.1785/0120000922

Jourdon, A., Pourhiet, L. L., Petit, C., & Rolland, Y. (2017). The deep structure and reactivation of the Kyrgyz Tien Shan: Modelling the past to better constrain the present. *Tectonophysics*, *746*, 530–548. https://doi.org/10.1016/j.tecto.2017.07.019

Kaneko, Y., & Fialko, Y. (2011). Shallow slip deficit due to large strike-slip earthquakes in dynamic rupture simulations with elastoplastic off-fault response. *Geophysical Journal International*, *186*(3), 1389–1403. https://doi.org/10.1111/j.1365-246x.2011.05117.x

Kulikova, G. (2016). Source parameters of the major historical earthquakes in the Tien-Shan region from the late 19th to the early 20th century. *PhD thesis, University of Potsdam*.

Langston, C. A. (1987). Depth of faulting during the 1968 Meckering, Australia, earthquake sequence determined from waveform analysis of local seismograms. *Journal of Geophysical Research: Solid Earth*, *92*(B11), 11561–11574. https://doi.org/10.1029/jb092ib11p11561

Li, S. Q., Wang, X., & Suppe, J. (2012). Compressional salt tectonics and synkinematic strata of the Western Kuça foreland basin, southern Tian Shan, China. *Basin Research*, *24*(4), 475–497. https://doi.org/10.1111/j.1365-2117.2011.00531.x

Li, Z. M., Li, W. Q., Li, T., Xu, Y. R., Su, P., Guo, P., et al. (2021). Seismogenic fault and coseismic surface deformation of the Maduo Ms7.4 earthquake in Qinghai, China: A quick report. *Seismology and Geology*, *43*(3), 722–737. (in Chinese with English abstract).

Letouzey, J., Colletta, B., Vially, R., & Chermette, J. C. (1995). Evolution of salt-related structures in compressional settings. In: M. P. A. Martin, D. G. Roberts, & S. Snelson, (Eds.) *Salt tectonics: A global perspective*. AAPG Memoir, 65: 41–60.

Long, F., Wen, X. Z., & Xu, X. W. (2006). Empirical relationships between magnitude and rupture length, and rupture area, for seismogenic active faults in North China. *Seismology and Geology*, *28*(4), 511–535. (in Chinese with English abstract).

Makarov, V. I., Alekseev, D. V., Batalev, V. Y., Bataleva, E. A., Belyaev, I. V., Bragin, V. D., et al. (2010). Underthrusting of Tarim beneath the Tien Shan and deep structure of their junction zone: Main results of seismic experiment along MANAS profile Kashgar-Song-Köl. *Geotectonics*, *44*, 102–126. https://doi.org/10.1134/S0016852110020020

Massonnet, D., Rossi, M., Carmona, C., Adragna, F., Peltzer, G., Feigl, K., & Rabaute, T. (1993). The displacement field of the Landers earthquake mapped by radar interferometry. *Nature*, *364*(6433), 138–142. https://doi.org/10.1038/364138a0

Molnar, P. (1988). Continental tectonics in the aftermath of plate tectonics. *Nature*, *335*(6186), 131–137. https://doi.org/10.1038/335131a0

Molnar, P., & Deng, Q. D. (1984). Faulting associated with large earthquakes and the average rate of deformation in central and eastern Asia. *Journal of Geophysical Research: Solid Earth*, *89*(B7), 6203–6227. https://doi.org/10.1029/jb089ib07p06203

Molnar, P., & Ghose, S. (2000). Seismic moments of major earthquakes and the rate of shortening across the Tien Shan. *Geophysical Research Letter*, *27*, 2377–2380. https://doi.org/10.1029/2000GL011637

Molnar, P., & Tapponnier, P. (1975). Cenozoic tectonics of Asia: Effects of a continental collision—Features of recent continental tectonics in Asia can be interpreted as results of the India-Eurasia collision. *Science*, *189*(4201), 419–426. https://doi.org/10.1126/science.189.4201.419

Okada, Y. (1985). Deformation due to shear and tensile faults in a half-space. *Bulletin of the Seismological Society of America*, *75*, 1135–1154. https://doi.org/10.1785/bssa0750041135

Pla, O., Roca, E., Xie, H. W., lzquierdo-Llavall, E., Munoz, J. A., Rowan, M. G., et al. (2019). Influence of syntectonic sedimentation and décollement rheology on the geometry and evolution of orogenic wedges: Analog modeling of the Kuqa fold-and-thrust belt (NW China). *Tectonics*, *38*, 2727–2755. https://doi.org/10.1029/2018tc005386

Roca, E., Sans, M., & Koyi, H. A. (2006). Polyphase deformation of diapiric areas in models and in the eastern Prebetics (Spain). *AAPG Bulletin*, *90*, 115–136. https://doi.org/10.1306/07260504096

Rosen, P. A., Hensley, S., Joughin, I. R., Li, F. K., Madsen, S. N., Rodriguez, E., & Goldstein, R. M. (2000). Synthetic aperture radar interferometry. *Proceedings of the IEEE*, *88*(3), 333–382. https://doi.org/10.1109/5.838084

Rowan, M. G., Lawton, T. F., Giles, K. A., & Ratiff, K. A. (2003). Near sal deformation in La Popa basin, Mexico, and the northern Gulf of Mexico; a general model for passive diapirism. *AAPG Bulletin*, *87*(5), 733–756. https://doi.org/10.1306/01150302012

Sadybakasov, I. (1990). *Neotectonics of high Asia* (p. 176). Russian Nauka. (in Russian).

Saint-Carlier, D., Charreau, J., Lavé, J., Blard, P.-H., Dominguez, S., Avouac, J.-P., et al. (2016). Major temporal variations in shortening rate absorbed along a large active fold of the southeastern Tianshan piedmont (China). *Earth and Planetary Science Letters*, *434*, 333–348. https://doi.org/10.1016/j.epsl.2015.11.041

Scholz, C. H. (1998). Earthquakes and friction laws. *Nature*, *391*, 37–42. https://doi.org/10.1038/34097

Schuster, D. C. (1995). Deformation of allochthonous salt and evolution of related salt-structural systems, eastern Louisiana Gulf Coast. In M. P. A. Jackson, D. G. Roberts, & S. Snelson (Eds.), (Vol. 65, pp. 177–198). AAPG Memoir. *Salt tectonics: A global perspective*.

Selander, J., Oskin, M., Ormukov, C., & Abdrakhmatov, K. (2012). Inherited strikeslip faults as an origin for basement-cored uplifts: Example of the Kungey and Zailiskey ranges, northern Tian Shan. *Tectonics*, *31*, TC4026. https://doi.org/10.1029/2011TC003002

Shen, Z. K., Wang, M., Li, Y. X., Jackson, D. D., Yin, A., Dong, D. A., & Fang, P. (2001). Crustal deformation along the Altyn-Tagh fault system, Western China, from GPS. *Journal of Geophysical Research*, *106*(B12), 30607–30621. https://doi.org/10.1029/2001JB000349

Stockmeyer, J. M., Shaw, J. H., Brown, N. D., Rhodes, E. J., Richardson, P. W., Wang, M., et al. (2017). Active thrust sheet deformation over multiple rupture cycles: A quantitative basis for relating terrace folds to fault slip rates. *The Geological Society of America Bulletin*, *129*, 1337–1356. https://doi.org/10.1130/B31590.1

Tang, M. Y., Liu, J., Shao, Y. X., Wang, P., & Yuan, Z.-D. (2015). Analysis about the minimum magnitude earthquake associated with surface ruptures. *Seismology and Geology*, *37*(4), 1193–1214. (in Chinese with English abstract).

Tang, P. C., Rao, G., Li, S. Q., & Yu, Y. L. (2018). The effect of salt thickness in fold lateral linkage: A case study of the anticlines in the leading edge of the Western Kuqa fold and thrust belt, south Tianshan. *Acta Geologica Sinica*, *92*(3), 437–448. (in Chinese with English abstract).

Tapponnier, P., & Molnar, P. (1979). Active faulting and Cenozoïc tectonics of the Tien Shan, Mongolia, and the Baïkal region. *Journal of Geophysical Research*, *84*, 3425–3459. https://doi.org/10.1029/jb084ib07p03425

Thompson, S. C., Weldon, R. J., Rubin, C. M., Abdrakhmatov, K., Molnar, P., & Berger, G. W. (2002). Late quaternary slip rates across the central Tien Shan, Kyrgyzstan, central Asia. *Journal of Geophysical Research: Solid Earth*, *107*(B9), 2203–2211. https://doi.org/10.1029/2001JB000596

Thompson Jobe, J. A., Li, T., Chen, J., Burbank, D. W., & Bufe, A. (2017). Quaternary tectonic evolution of the Pamir-Tian Shan convergence zone, Northwest China. *Tectonics*, *36*, 2748–2776. https://doi.org/10.1002/2017TC004541

Wang, C., Ding, X., Li, Q., & Jiang, M. (2014). Equation-based on InSAR data quadtree downsampling for earthquake slip distribution inversion. *IEEE Geoscience and Remote Sensing Letters*, *11*(12), 2060–2064. https://doi.org/10.1109/LGRS.2014.2318775

Wang, M., & Shen, Z. K. (2020). Present-day crustal deformation of continental China derived from GPS and its tectonic implications. *Journal of Geophysical Research: Solid Earth*, *125*, e2019JB018774. https://doi.org/10.1029/2019JB018774

Wang, R. J., Diao, F., & Hoechner, A. (2013). SDM-A geodetic inversion code incorporating with layered crust structure and curved fault geometry. In *Proceedings of the general Assembly European Geosciences union, Vienna, Austria, 7–12 April 2013*.

Wang, X., John, S., Guan, S. W., Hubert-Ferrari, A., Gonzalez-Mieres, R., & Jian, C. (2011). Cenozoic structure and tectonic evolution of the Kuqa fold belt, southern Tianshan, China. *American Association of Petroleum*, *94*, 215–243. https://doi.org/10.1306/13251339M94389

Werner, C., Wegmüller, U., Strozzi, T., & Wiesmann, A. (2002). *Processing strategies for phase unwrapping for INSAR applications, Proc. EUSAR 2002, June* (pp. 4–6).

Worrall, D. M., & Snelson, S. (1989). Evolution of the northern Gulf of Mexico, with emphasis on Cenozoic growth faulting and the role of salt. In A. W. Bally, & A. R. Palmer (Eds.), *The geology of north America—An overview* (pp. 97–138). Geological Society of America. A.

Wu, C., Ren, G., Yu, J., Zheng, W., Li, X., Liu, J., et al. (2020). Oblique right-lateral faulting along the northern margin of the Ili Basin in the northern Tian Shan, northwest China. *Tectonics*, *39*(10), e2020TC006061. https://doi.org/10.1029/2020TC006061

Wu, C., Zheng, W., Zhang, P., Zhang, Z., Jia, Q., Yu, J., et al. (2019). Oblique thrust of the Maidan fault and late quaternary tectonic deformation in the southwestern Tian Shan, northwestern China. *Tectonics*, *38*, 2625–2645. https://doi.org/10.1029/2018TC005248

Wu, C. Y., Wu, G. D., Shen, J., Chen, J. B., Ali, M. J., & Chang, X. D. (2014). The late-Quaternary activity of the Nalati fault and its implications for the crustal deformation in the interior of the Tianshan mountains. *Quaternary Science*, *34*(2), 269–280. (in Chinese with English abstract).

Xu, X. H., Tong, X. P., Sandwell, D. T., Milliner, C., Dolan, J. F., James, H. et al. (2016). Refining the shallow slip deficit. *Geophysical Journal International*, *204*(3), 1867–1886. https://doi.org/10.1093/gji/ggv563

Yang, J., Zhu, H., Lay, T., Niu, Y., Ye, L., Lu, Z., et al. (2021). Multifault opposing-dip strike-slip and normal fault rupture during the 2020 Mw6.5 Stanley, Idaho earthquake. *Geophysical Research Letters*, *48*, e2021GL092510. https://doi.org/10.1029/2021GL092510

Yang, S. M., Li, J., & Wang, Q. (2008). The deformation pattern and fault rate in the Tianshan Mountains inferred form GPS observations. *Science in China - Series D: Earth Sciences*, *51*(8), 1064–1080. (in Chinese). https://doi.org/10.1007/s11430-008-0090-8

Yao, Y., Song, H. P., Chen, J. B., Li, S., & Jia, H. L. (2018). Late Quaternary tectonic activity and shortening rate of the Beiluntai fault zone in the South Tianshan, Xinjiang, NW China. *Arabian Journal of Geosciences*, *11*(14), 1–13. https://doi.org/10.1007/s12517-018-3717-x

Yin, A., Nie, S., Craig, P., Harrison, T. M., Ryerson, F. J., Qian, X. L., & Geng, Y. (1998). Late Cenozoic tectonic evolution of the southern Chinese Tian Shan. *Tectonics*, *17*(1), 1–27. https://doi.org/10.1029/97TC03140

Zhan, Y., Liang, M. J., Sun, X. Y., Huang, F. P., Zhao, L. Q., Gong, Y., et al. (2021). Deep structure and seismogenic pattern of the 2021.5.22 Madoi (Qinghai) MS7.4 earthquake. *Chinese Journal of Geophysics*, *64*(7), 2232–2252. (in Chinese with English abstract). https://doi.org/10.6038/cjg2021O0521

Zhang, P. Z., Deng, Q. D., Yang, X. P., Peng, S. Z., Xu, X. W., & Feng, X. Y. (1996). Late Cenozoic tectonic deformation and mechanism along the Tianshan Mountain, northwestern China. *Earthquake Research in China*, *12*(2), 127–140. (in Chinese with English abstract).

Zhang, P. Z., Deng, Q. D., Zhang, G. M., Ma, J., Gan, W. J., Min, W. et al. (2003). Active tectonic blocks and strong earthquakes in the continent of China. *Science in China - Series D: Earth Sciences*, *46*(2), 13–24.

Zhang, P. Z., Shen, Z. K., Wang, M., Gan, W. J., Burgmann, R., Molnar, P., et al. (2004). Continuous deformation of the Tibetan plateau form global positioning system data. *Geology*, *32*(9), 809–812. https://doi.org/10.1130/G20554.1

Zhou, D. M. (2013). *Characteristics of present-day crustal deformation and seismic hazard analysis in the western and central Tian Shan*. Ph.D. Dissertation of Institute of Geology. (in Chinese).

Zubovich, A. V., Wang, X., Scherba, Y. G., Schelochkov, G. G., Reilinger, R., Reigber, C., et al. (2010). GPS velocity field of the Tien Shan and surrounding regions. *Tectonics*, *29*, TC6014. https://doi.org/10.1029/2010TC002772